Flow, Turbulence and Combustion (2022) 109:1195–1213
https://doi.org/10.1007/s10494-022-00352-8

Direct numerical simulations of turbulent channel flow over ratchet roughness

Angela Busse[1] · **Oleksandr Zhdanov**[1]

Received: 3 March 2022 / Accepted: 12 July 2022 / Published online: 9 August 2022

Abstract
The influence of the orientation of ratchet-type rough surfaces on their fluid dynamic roughness effect is investigated using direct numerical simulations of turbulent channel flow at $Re_\tau = 395$. The ratchet length-to-height ratio is varied from $\ell/k = 2$ to 16 for a fixed ratchet height of $k/\delta = 0.1$ where δ is the mean channel half-height. The results show that both roughness function and mean flow and turbulence statistics strongly depend on the ratchet orientation. Existing empirical formulae, which estimate the roughness function ΔU^+ or the equivalent sand-grain roughness k_s based on surface-slope related parameters such as the effective slope or the Sigal-Danberg parameter, fail to accurately predict the differences between ratchet surfaces with high windward slopes and ratchet surfaces with high leeward slopes.

Keywords Turbulence · Channel flow · Rough walls · Direct numerical simulation

1 Introduction

It is well-established that not only the roughness height but also the topography of a surface, i.e., the spatial distribution and shape of roughness features, have a strong influence on its fluid dynamic roughness effect (Chung et al. 2021). However, many aspects of the topography-dependence of rough-wall turbulence are still not understood, and progress is made more difficult by the fact that different ways to parameterise the topographies of rough surfaces are used in different contexts. For example, the roughness function has been shown to increase with the effective slope ES (Napoli et al. 2008), which is defined as the plane-average of the absolute value of the local streamwise slope of the surface height map $h(x, y)$:

✉ Angela Busse
angela.busse@glasgow.ac.uk

Oleksandr Zhdanov
oleksandr.zhdanov@glasgow.ac.uk

[1] James Watt School of Engineering, University of Glasgow, University Avenue, Glasgow G12 8QQ, Scotland, United Kingdom

$$ES = \frac{1}{A} \int \int \left| \frac{\partial h(x,y)}{\partial x} \right| dxdy, \tag{1}$$

where x is the streamwise, y the spanwise coordinate, and A is the total planform area of the surface. The effective slope is directly related to the frontal solidity of a surface by $\lambda_f = ES/2$ (MacDonald et al. 2016), which is defined as the projected frontal area of the roughness per unit planform area (Schlichting 1936).

The Sigal-Danberg parameter Λ_s (Sigal and Danberg 1990, van Rij et al. 2002) also effectively characterises the streamwise slope of a rough surface, but in contrast to ES and λ_f it distinguishes between the windward (positive slope) and the leeward (negative slope) faces of a rough surface. It is computed as

$$\Lambda_s = \lambda_f^{-1} \left(\frac{A_f}{A_w} \right)^{-1.6}, \tag{2}$$

where A_f is the frontal projected area of the roughness elements and A_w is their total windward wetted surface area.

For bluff bodies the orientation of the body with respect to the mean flow direction has a strong influence on their roughness effect, e.g., a triangular prism will experience much higher drag if its side is facing the flow when compared to a triangular prism with an edge facing the flow (see, e.g., Seyed-Aghazadeh et al. 2017). Therefore, it could be expected that the drag of asymmetric roughness elements, e.g., a roughness element with differing windward and leeward slope, is also orientation dependent. While many rough surfaces have slope distributions with zero skewness, examples for roughness with different leeward and windward slopes can be found in a geophysical context, e.g., transverse sand dunes and ripples (Gao et al. 2015) and some forms of ocean waves (Longuet-Higgins 1982).

The simplest form of roughness where an imbalance between windward and leeward geometry occurs is two-dimensional ratchet roughness. Recent experiments on turbulent convection by Jiang et al. (2018) demonstrated that the orientation of ratchet-type roughness, a form of 2D transverse roughness where the magnitude of the leeward slope strongly differs from the windward slope, has strong influence on large-scale convective structures.

This poses the following questions: How important is it to include the sign of the local surface slope relative to the mean flow direction in the corresponding parameter definition? Is the Sigal-Danberg parameter or the effective slope / frontal solidity better suited for capturing the influence of surface slope on the roughness effect?

In this paper, turbulent channel flow over two-dimensional ratchet roughness is investigated using direct numerical simulations to address the above questions. In Sect. 2 the studied ratchet geometries are described and details of the simulation setup are presented. The dependency of the roughness function, mean flow and turbulence statistics, and the mean flow fields on ratchet length and orientation are discussed in Sect. 3. Conclusions are summarised in Sect. 4.

2 Methodology

Direct numerical simulations (DNS) of incompressible turbulent channel flow are conducted over systematically varied ratchet-type roughness to investigate the relative influence of windward faces (positive slope) and leeward faces (negative slope) of a rough surface on mean flow and turbulence statistics.

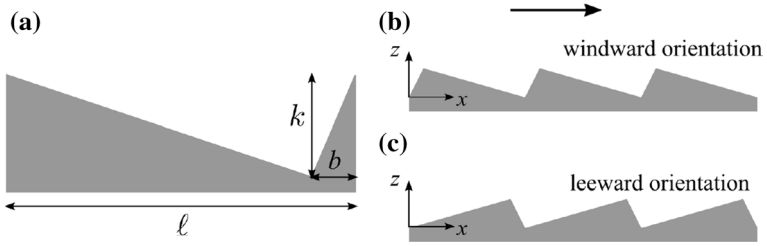

Fig. 1 (**a**) Schematic illustration of the basic geometric parameters of the ratchet roughness; (**b**) windward orientation and (**c**) leeward orientation of the ratchet pattern. The black arrow indicates the direction of the mean flow

Table 1 Overview of investigated ratchet surfaces. The sketches show the ratchet pattern over a streamwise length of 1.6δ. Key surface topographical parameters are the effective slope ES and the Sigal-Danberg parameter Λ_s. The line styles that are used in the profile plots in Sect. 3 are also shown

ℓ	orientation	sketch	ES	Λ_s	line style
$2k$	windward		1	2.10	
$2k$	leeward		1	6.14	
$4k$	windward		0.5	4.78	
$4k$	leeward		0.5	31.6	
$8k$	windward		0.25	13.9	
$8k$	leeward		0.25	183	
$12k$	windward		0.167	30.8	
$12k$	leeward		0.167	520	
$16k$	windward		0.125	58.0	
$16k$	leeward		0.125	1096	

Five different surfaces composed of spanwise bars of triangular cross-section were investigated. The height of the triangular cross-section, k, was set to 0.1δ in all cases, where δ is the mean channel half-height. The length of the triangular cross-section, ℓ, was varied from $2k$ to $16k$. In each case, one side of the triangular cross-section had a higher slope $k/(\ell/8)$ than the other $k/(7\ell/8)$ to create a ratchet-type rough surface (see Table 1).

Each surface was studied in two different orientations: (a) windward orientation of the high-slope side and (b) leeward orientation of the high-slope side of the triangular cross-section (see Fig. 1).

All simulations were conducted at friction Reynolds number $Re_\tau = u_\tau\delta/\nu = 395$ with a constant mean streamwise pressure gradient using the code iIMB (Busse et al. 2015), where the roughness was resolved using an iterative version of the embedded boundary method by Yang and Balaras (2006). The simulation parameters are summarised in Table 2. The domain size allows four repetitions of the ratchet pattern in the streamwise direction for the longest ratchet pattern with $\ell = 16k$. For the ratchet surfaces with $\ell = 12k$ the streamwise domain size was increased to $L_x = 7.2\delta$, to be able to fit an integer number of repetitions of the ratchet pattern into the domain.

The same ratchet pattern was applied to both the upper and the lower wall of the channel; the pattern on the upper wall was shifted by $\ell/2$ to minimize any local blockage

Table 2 Simulation parameters for the direct numerical simulations. L_x: domain size in streamwise direction; L_y: domain size in spanwise direction; L_z: domain size in wall-normal direction; $N_x \times N_y \times N_z$: grid size; Δx^+: grid spacing in streamwise direction; Δy^+: grid spacing in spanwise direction; Δz^+_{min}: minimum wall-normal grid spacing; Δz^+_{max}: maximum wall-normal grid spacing

	L_x/δ	L_y/δ	L_z/δ	$N_x \times N_y \times N_z$	Δx^+	Δy^+	Δz^+_{min}	Δz^+_{max}
$\ell = 2k$	6.4	3.2	2.1	$4096 \times 256 \times 432$	0.62	4.94	0.67	4.22
$\ell = 4k$	6.4	3.2	2.1	$2048 \times 256 \times 432$	1.23	4.94	0.67	4.22
$\ell = 8k$	6.4	3.2	2.1	$1024 \times 256 \times 432$	2.47	4.94	0.67	4.22
$\ell = 12k$	7.2	3.2	2.1	$1152 \times 256 \times 432$	2.47	4.94	0.67	4.22
$\ell = 16k$	6.4	3.2	2.1	$1024 \times 256 \times 432$	2.47	4.94	0.67	4.22
Smooth	8.0	4.0	2.0	$640 \times 320 \times 360$	4.94	4.94	0.50	3.98

effects. The shift on the upper wall did not introduce any significant tilt to the local mean flow, the maximum absolute value of the time, phase, and spanwise averaged wall-normal velocity field at the channel centre max ($|\bar{w}(x, z = \delta)|$) was below $0.05u_\tau$ in all cases. Periodic boundary conditions were imposed in the streamwise and spanwise direction. The reference plane $z = 0$ corresponds to the mean roughness height, i.e., $\langle h(x) \rangle = 0$, where $h(x)$ is the two-dimensional roughness profile. Grid spacing in the x-direction was adjusted to ensure each ratchet was resolved by at least 128 grid points per repeating unit. A constant grid spacing consistent with smooth-wall resolution criteria was used in the spanwise direction since the surface topography is independent of y. The wall-normal grid spacing was set to Δz^+_{min} across the height of the ratchet and was gradually increased above, reaching its maximum Δz^+_{max} at the channel centre. After the flow had attained a statistically stationary state, statistics were averaged over a minimum of fifty flow through times $L_x/\overline{U}$, where $\overline{U}$ is the bulk-flow velocity. For the calculation of the Reynolds and dispersive stresses, spanwise averages and spatial phase averages over the repetitions in the ratchet pattern were applied. Simulation parameters for a smooth-wall simulation at $Re_\tau = 395$, which is used as a reference case in the following, are also included in Table 2 (Jelly and Busse 2019).

3 Results and Discussion

In this section, first the roughness effect of the ratchet surfaces is quantified and compared to empirical predictions from the literature. This is followed by a discussion of mean flow and turbulence statistics and the time averaged flow fields.

3.1 Roughness Function and Equivalent Sand-Grain Roughness

Results for the Hama roughness function ΔU^+ (Hama 1954) and the bulk flow velocity $\overline{U}$ are included in Table 3. Based on their ΔU^+ values, all cases fall into the upper transitionally to fully rough regime. In Fig. 2a, ΔU^+ is shown as a function of the effective slope ES. For comparison, data from the large-eddy simulations of Napoli et al. (2008) for flow over two-dimensional irregular sinusoidal roughness, data by Chan et al. (2015) for regular 3D sinusoidal 'egg-carton' roughness, data by De Marchis (2016) for triangular waves, and data by Kuwata and Nagura (2020) for positively and negatively skewed

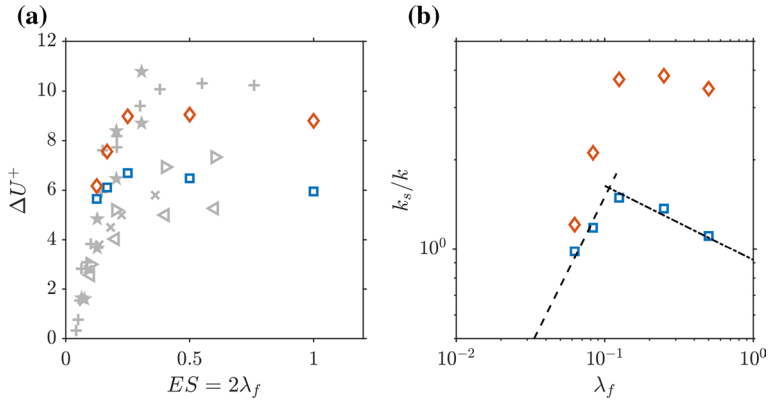

Fig. 2 (**a**) Roughness function versus effective slope for ratchet surfaces in leeward orientation (blue squares) and in windward orientation (orange diamonds). Grey symbols show data for different roughness types from the literature for comparison, +: 2D irregular wavy surfaces (Napoli et al. 2008); ×: regular 3D sinusoidal surfaces (Chan et al. 2015), ⋆: triangular waves (De Marchis 2016), ◁ negatively skewed irregular 3D roughness (Kuwata and Nagura 2020), ▷: positively skewed irregular 3D roughness (Kuwata and Nagura 2020) (**b**) Estimate for the equivalent sand-grain roughness k_s as a function of the frontal solidity λ_f; the blue squares show the results for the ratchets in leeward orientation and the orange diamonds the results for the windward orientation. The dashed black line indicates $\sim \lambda_f^{+1}$ and the dash-dotted black line $\sim \lambda_f^{-1/4}$

Table 3 Measured values for bulk-flow velocity $\overline{U}$, roughness function ΔU^+, and the zero-plane offset z_{off} for the virtual origin of the logarithmic profile relative to the roughness mean plane (based on a manual fit to the expected slope in the logarithmic region). The equivalent sand-grain roughness k_s was estimated using relationship (3). Also shown is the predicted value for roughness function ΔU^+ using relationship (4) and the predicted value for equivalent sand-grain roughness using relationship (5)

ℓ	orientation	$\overline{U}$	z_{off}/δ	ΔU^+	k_s/k	ΔU^+_{pred}	$(k_s/k)_{\text{pred}}$
$2k$	Windward	8.78	0.02	8.80	3.47	9.58	0.124
$2k$	Leeward	11.22	0.03	5.95	1.11	9.58	8.0
$4k$	Windward	8.63	0.0	9.05	3.83	7.85	7.13
$4k$	Leeward	10.87	0.02	6.48	1.37	7.85	2.98
$8k$	Windward	9.15	− 0.06	8.98	3.73	6.12	7.59
$8k$	Leeward	10.88	0.0	6.69	1.49	6.12	0.40
$12k$	Windward	10.60	− 0.08	7.56	2.11	5.11	3.07
$12k$	Leeward	11.42	0.0	6.16	1.21	5.11	0.12
$16k$	Windward	12.06	− 0.09	6.17	1.21	4.39	1.49
$16k$	Leeward	11.97	0.0	5.65	0.98	4.39	0.05

irregular roughness is shown. For moderate *ES*, the roughness function increases with *ES*, which is consistent with the observations of Napoli et al. (2008), Schultz and Flack (2009), and others (De Marchis 2016, Forooghi et al. 2017, Busse and Jelly 2020, Kuwata and Nagura 2020). For the ratchets with $\ell/k = 16$, ΔU^+ is not very sensitive to the orientation: the windward oriented surface yields only a slightly higher roughness effect than the leeward oriented case with difference in ΔU^+ below 10%. The roughness function reaches its

maximum between $\ell/k = 8$ and $\ell/k = 4$ which corresponds to effective slopes of 0.25 to 0.5. For the cases with $ES \geq 0.25$ the effect of the orientation with respect to the mean flow is much stronger - the roughness function of the windward oriented ratchets is 30% to 40% higher compared to the leeward oriented cases.

As ES is increased above 0.35, a saturation of the roughness function would be expected (Napoli et al. 2008, Schultz and Flack 2009) as can for example be seen in the data of Napoli et al. (2008) included in Fig. 2a. For the ratchet surfaces a gradual decrease of ΔU^+ can be observed. This decrease in ΔU^+ with ES for high ES is much weaker than the difference in ΔU^+ induced by the change in orientation. Variations in the roughness effect in the high effective slope regime ($ES \geq 0.35$) are often a result of a change in surface skewness (Chung et al. 2021), as is also evident from the data by Kuwata and Nagura (2020) included in Fig. 2a. However, the current surfaces are all neutrally skewed (as are the 3D sinusoidal surfaces by Chan et al. (2015) and the triangular waves by De Marchis (2016)). The present surfaces can thus serve as an example for the fact that further topographical aspects, such as orientation, can influence the roughness effect in the high effective slope regime.

Further insight in the behaviour in the high slope regime can be gained by considering the dependency of the equivalent sand-grain roughness on the frontal solidity λ_s, which is directly related to effective slope as discussed above. To fully establish the equivalent sand-grain roughness of a surface, measurements need to be taken for a range of k^+ values to ascertain that the fully-rough limit has been attained (Jiménez 2004; Schultz and Flack 2009; Busse et al. 2017; Thakkar et al. 2018). However, when using DNS this is difficult to achieve due to the rapidly rising computational cost as the Reynolds number is increased (Pope 2000). Therefore, we follow the standard approach applied in DNS-based roughness parameter studies and obtain an estimate for the equivalent sand-grain roughness based on the measured value of the roughness function at a single Reynolds number (Forooghi et al. 2017; Kuwata and Nagura 2020; Sarakinos and Busse 2022). The equivalent sand-grain roughness has been calculated from ΔU^+ following the approach discussed by Chung et al. (2021)

$$\frac{k_s}{k} = \frac{\exp\left(\kappa\left(\Delta U^+ - A + B_s(\infty)\right)\right)}{k^+}, \tag{3}$$

where $A - B_s(\infty) \approx -3.5$ and $\kappa \approx 0.4$.

As shown in Fig. 2b, this recovers a familiar pattern (Jiménez 2004). For small frontal solidity, the equivalent sand-grain roughness increases, and for high frontal solidity k_s decreases. The location of the maximum at $\lambda_f = 0.125$ to 0.25 falls into the range of maximum locations reported in the reviews by Jiménez (2004) and Chung et al. (2021). However, whilst for low λ_f the equivalent sand-grain roughness of the leeward cases increases approximately with λ_f^{+1} in agreement with the data summarized by Jiménez (2004), a steeper increase is observed for the windward oriented cases. Furthermore, the decrease of k_s at high λ_f is much more gradual with $k_s/k \sim \lambda_f^{-1/4}$ than the $k_s/k \sim \lambda_f^{-2}$ estimated by Jiménez (2004). It should be noted, that in many cases a decrease in k_s/k at high frontal solidities is connected to a decrease in surface skewness, as more and more roughness elements are placed on the surfaces (see, e.g., Schlichting (1936), Macdonald et al. (1998), Sarakinos and Busse (2022)). As discussed above, all of the ratchet surfaces are neutrally skewed, so the decrease of k_s/k cannot be attributed to skewness effects in the present case. A decrease in the roughness effect for neutrally skewed surfaces with high frontal solidity

was previously reported in the study by MacDonald et al. (2018) who found for tall, neutrally skewed bar roughness a scaling of $k_s/k \sim \lambda_f^{-1}$ in the 'very dense' regime for $\lambda_f \geq 1.5$. The high λ_f cases of the current study fall into the 'dense' regime, i.e., the regime below the 'very dense' regime, where k_s/k dependency on λ_f is expected to be strongly influenced by roughness geometry (MacDonald et al. 2018). This may account for the more gradual decrease in k_s/k with λ_f for the ratchet surfaces. Investigations for even shorter ratchets would be required to establish whether a scaling similar to the one observed by MacDonald et al. (2018) would be approached in the 'very dense' regime.

A key aim of this study is to evaluate how well existing empirical correlations can predict the roughness effects of orientation-dependent roughness such as ratchet surfaces. Due to their symmetry with respect to a reflection with respect to the x-axis, the skewness Ssk of all ratchet surfaces considered here is zero. Therefore, we focus in the following on correlations that mainly account for effects of surface slope, i.e., correlations that contain ES or Λ_s as a key topographical parameter. De Marchis et al. (2020) developed an empirical correlation for the dependency of ΔU^+ on surface topography

$$\Delta U^+ = \frac{1}{\kappa} \ln(ES \cdot Sq^+) + B, \tag{4}$$

where Sq is the rms roughness height and $B = 3.5$ is an empirical constant. This fit was based on data for two- and three-dimensional random sinusoidal roughness (De Marchis et al. 2020; De Marchis 2016; Napoli et al. 2008), triangular waves (De Marchis et al. 2020), the data of (Thakkar et al. 2017) based on scans of engineering roughness, and the data of Chan et al. (2015) for regular 3D sinusoidal 'egg-carton' roughness. For the present ratchet surfaces the rms roughness height is given by $Sq = k/(2\sqrt{3})$, i.e., $Sq \approx 0.0289\delta$.

Sigal and Danberg (1990) proposed the following relationship for the equivalent sand-grain roughness for two-dimensional roughness:

$$\frac{k_s}{k} = \begin{cases} 0.003215\Lambda_s^{4.925} & 1.4 \leq \Lambda_s \leq 4.89 \\ 8.0 & 4.89 < \Lambda_s < 13.25 \\ 151.71\Lambda_s^{-1.1379} & 13.25 \leq \Lambda_s \leq 100 \end{cases} \tag{5}$$

For the purposes of this study the upper bound of the third branch of the Sigal-Danberg relationship has been extended above $\Lambda_s = 100$ which is consistent with Fig. 2 in Sigal and Danberg's paper (Sigal and Danberg 1990). Figure 3a shows the estimated equivalent sand-grain roughness values of the present cases compared to the above relationship.

It is evident from Table 3 and Figs. 3a, 4a and b that neither of the empirical relationships gives a satisfactory prediction for the roughness effect of ratchet surfaces. The relationship by Sigal and Danberg significantly overpredicts five of the values and significantly underpredicts four of them; only one value is close to the actual value. The modified Sigal-Danberg relationship for three-dimensional irregular roughness by van Rij et al. (2002) was also tested (not shown), but this led to a significant underprediction of the equivalent sand-grain roughness in almost all cases, and it thus does not improve outcomes compared to the original relationship (5) for two-dimensional roughness. The relationship by Sigal and Danberg performs especially poorly for the three longest ratchets in leeward orientation, for which it strongly underpredicts the roughness effect. This can be related to the fact that the law-of-the wall intercept for these surfaces shows a much more gradual decrease with Λ_s than the experimental data that Sigal and Danberg used for the development of their

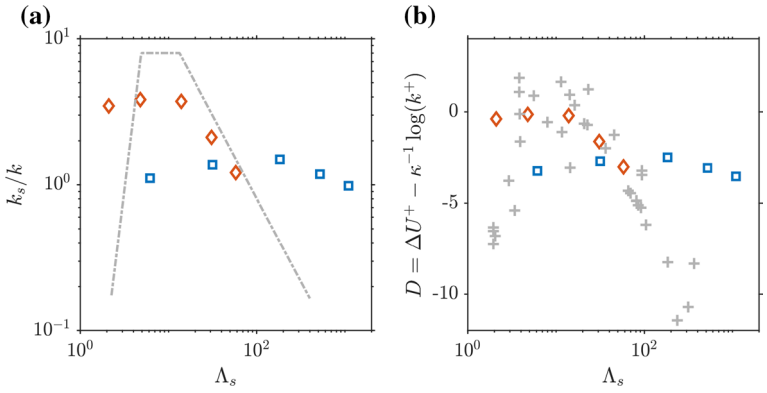

Fig. 3 (**a**) Estimate for the equivalent sand-grain roughness k_s as a function of the Sigal-Danberg parameter Λ_s; the blue squares show the results for the ratchets in leeward orientation and the orange diamonds the results for the windward orientation; the grey dash-dotted line shows the Sigal-Danberg relationship (5). (**b**) Law of the wall intercept versus Λ_s; blue and orange symbols as in part (a); the grey crosses show experimental data assembled by Sigal and Danberg (1990) from various sources on which they based their empirical correlation

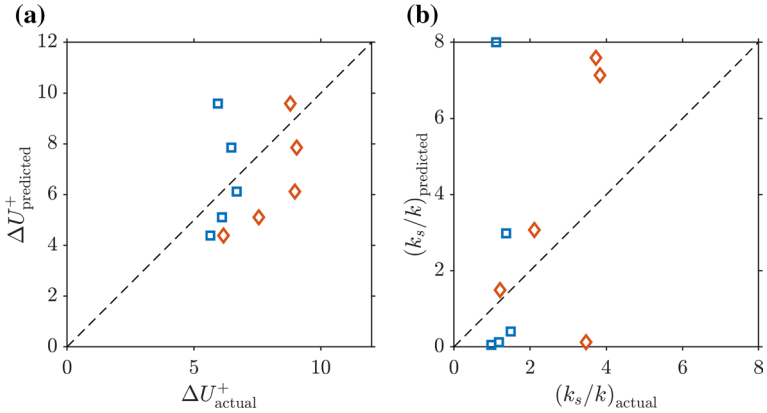

Fig. 4 (**a**) Value predicted by (4) versus measured value of the roughness function ΔU^+. (**b**) Value predicted by (5) versus measured value for the equivalent sand-grain roughness. Blue squares indicate data for surfaces in leeward orientation, orange diamonds for surfaces in windward orientation

empirical correlation (see Fig. 3b). In comparison, the high Λ_s cases in windward orientation show a better agreement with the trend predicted by equation (5).

The relationship by De Marchis et al. (4) performs reasonably well at predicting some of the moderate effective slope cases, but it cannot capture the decrease in ΔU^+ that is observed for high frontal solidity since the empirical relationship (4) predicts a monotonic increase with *ES* for a fixed value of *Sq*. Furthermore, relationship (4) cannot distinguish between windward and leeward oriented cases since *ES* is by definition insensitive to the sign of the local surface slope.

Comparing the two tested empirical correlations, the relationship by De Marchis et al. (4) yields a normalised root-mean square error (NRMSE) of 0.52 (using the

average of observed values for the normalisation), which, while it is substantial, is still significantly smaller than the NRSME of 4.45 for the Sigal and Danberg relationship (5). The fit of the empirical relationship by De Marchis et al. (4) could be somewhat improved by making the only adjustable parameter, i.e., the constant B, orientation dependent, by relating it to a parameter such as the skewness of the streamwise slope distribution $Ssk_{\partial h/\partial x}$, which is positive ($Ssk_{\partial h/\partial x} \approx 2.27$) for all considered windward oriented cases and negative ($Ssk_{\partial h/\partial x} \approx -2.27$) for all leeward oriented cases. However, the fundamental issue that cannot be overcome by this approach is the saturation and gradual decrease of ΔU^+ for high effective slope, since (4) will always predict a monotonic increase with ES, provided the other parameters, such as Sq, are fixed.

3.2 Mean Velocity Profiles

Clear influence of the ratchet orientation can also be observed in the mean flow profiles and the Reynolds and dispersive stress profiles. In the mean-streamwise velocity profile, shown in Fig. 5a, a zero-plane offset z_{off} had to be applied for most cases with high windward slope to recover the expected slope in the log-region, whereas z_{off} is approximately zero for almost all of the leeward-oriented cases (see Table 3).

For the windward oriented cases z_{off} decreases from a positive value to a negative value with increasing ratchet length ℓ. For the longer ratchets $\ell/k \geq 8$ in windward orientation, the virtual origin of the roughness is effectively below the bottom of the ratchets. In contrast, the virtual origin of the ratchets in leeward orientation corresponds to the roughness mean plane for $\ell/k \geq 8$. This illustrates the strong dependence of the mean flow on the orientation of the ratchet surfaces even in the case $\ell/k = 16$, where only weak orientation impact on ΔU^+ is observed. This observation is also reflected in the velocity defect profiles (see Fig. 5b), where a deviation from the smooth-wall data can be observed to higher wall-normal locations for the long ratchets in windward orientation. The collapse of the profiles for the long ratchets in windward orientation on the smooth-wall profile can be significantly improved by the application of the offset, but the collapse remains superior, i.e., extends closer to the wall, for long ratchets in leeward orientation (see inset to Fig. 5b). Based on the results by Krogstad and Efros (2012) for two-dimensional transverse bar

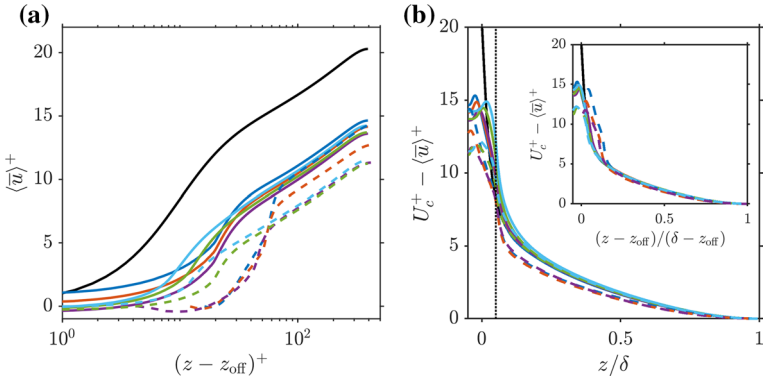

Fig. 5 (**a**) Semi-logarithmic velocity profiles; (**b**) velocity defect profiles. Line styles and symbols as shown in Table 1. The thick black line indicates the smooth wall reference case. The thin dotted vertical line indicates the height of the roughness crests

roughness, a recovery of outer-layer similarity would be expected for high Reynolds number and high δ/k (Flack and Schultz 2014). The current results show, that in addition to δ/k and Re_τ, which are fixed for the current simulations, the recovery of outer-layer similarity is also influenced by roughness orientation in the case of orientation-dependent roughness.

3.3 Reynolds Stress Statistics

No zero-plane offset was applied to the Reynolds stresses, since an almost perfect collapse on the smooth-wall reference case can be observed in the Reynolds shear stress profiles for $z/\delta \gtrapprox 0.2$ (Fig. 6a). Overall, a good collapse in the outer layer was also observed for the streamwise and wall-normal Reynolds stress profiles (see Fig. 6b and c), although some deviations can be observed for the longer ratchets in windward orientation. Clear deviations from outer-layer similarity can be observed for the spanwise Reynolds stress profiles, where the three longest ratchets in windward orientation show significant deviations from the smooth-wall profile in the outer part of the profile (see Fig. 6d).

The Reynolds shear stress shows for the long ratchets $\ell \geq 8k$ in leeward orientation elevated levels immediately above the rough surfaces compared to the smooth-wall case. Peak Reynolds shear stress levels are for these cases higher for ratchets in leeward orientation compared to ratchets in windward orientation, although the difference between peak levels

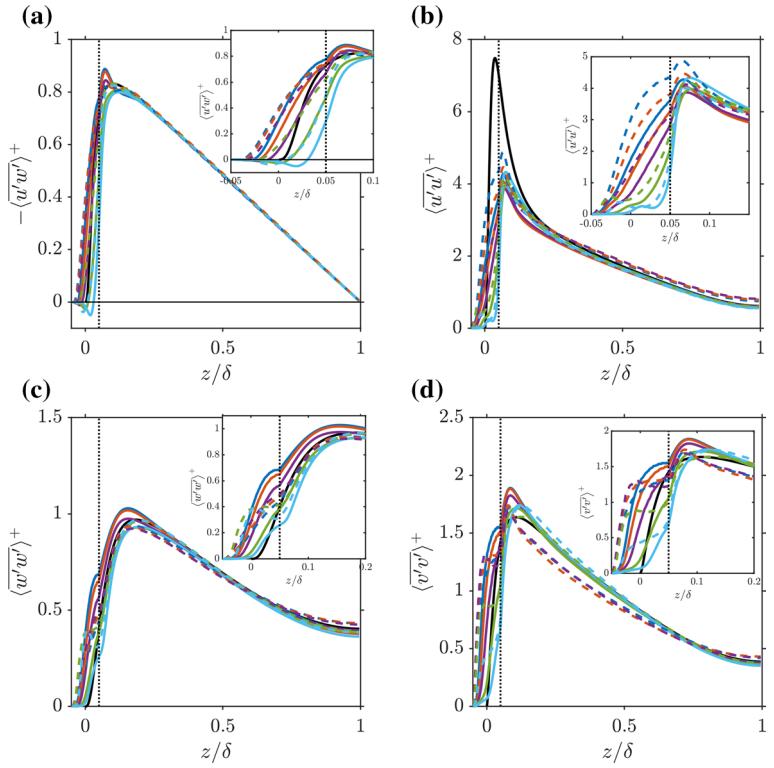

Fig. 6 (**a**) Reynolds shear stress; (**b**) streamwise Reynolds stress; (**c**) wall-normal Reynolds stress; (**d**) spanwise Reynolds stress. Line styles and symbols as shown in Table 1. The thick black line indicates the smooth wall reference case. The thin dotted vertical line indicates the height of the roughness crests

decreases with decreasing ratchet length. In contrast, for the short ratchets $\ell \leq 4k$ peak levels in Reynolds shear stress are in all cases lower than in the smooth-wall case, the windward oriented ratchets show higher peak levels compared to the leeward oriented cases, and the difference in peak levels for the two orientations increases as the ratchet length is decreased. Within the ratchet cavities, Reynolds shear stresses tend to be higher for ratchets in windward orientation and increase with increasing ratchet length. For the short ratchets negative values of the Reynolds shear stress can be observed within the cavities, most prominently for the $\ell = 2k$ case in leeward orientation.

The streamwise Reynolds stresses (Fig. 6b) show a clear reduction of the peak values compared to the smooth wall reference case, which is consistent with observations for other roughness forms (see, e.g., (Forooghi et al. 2018, Busse and Jelly 2020)). The peak values are higher for ratchets in windward orientation, except for the shortest ratchet $\ell = 2k$ where the leeward oriented case attains higher streamwise Reynolds stress values. Peak levels decrease for the longer ratchets with decreasing ratchet length; this trend is reversed for the shortest ratchets, where an increasing trend is observed. Within the ratchet cavities there is also a clear dependency of $\langle\overline{u'u'}\rangle$ on the ratchet length ℓ and orientation. Streamwise velocity fluctuations are significantly higher for ratchets in windward orientation, this difference is more pronounced for the longer ratchets. Furthermore, the level of streamwise velocity fluctuations is higher for longer ratchets. An increase in streamwise velocity fluctuations within a rough surface with increasing size of roughness features in the streamwise direction has also been observed for other surfaces, e.g., for anisotropic irregular Gaussian roughness (Busse and Jelly 2020).

The wall-normal Reynolds stresses (Fig. 6c)) also show higher levels for longer ratchets. For the peak levels some of the trends observed for $\langle\overline{u'u'}\rangle$ and $-\langle\overline{u'w'}\rangle$ are reversed, namely for the long ratchets the leeward orientation gives rise to higher $\langle\overline{w'w'}\rangle$ peaks than the windward orientation, whereas for short ratchets the opposite is the case. A similar trend is also observed for the wall-normal Reynolds stress levels within the cavities.

Peak levels of spanwise velocity fluctuations are consistently higher for ratchets in leeward orientation. For longer ratchets, this peak location is shifted closer to the wall and occurs just above the roughness crests. For the shorter ratchet cases, the peak location is at the same location as for the smooth wall case or further away from the wall. In the upper part of the ratchet cavities, spanwise Reynolds stresses continue to be higher for the leeward oriented cases. This trend is reversed in the lower part of the ratchet cavities, where higher spanwise Reynolds stresses are observed for the windward oriented cases.

Considering the above observations, the Reynolds stress levels significantly altered for all ratchet cases; Reynolds stress levels attain appreciable values within the ratchet cavities in all cases, although the interaction with the lower part of the roughness cavity appears to be higher for the windward oriented cases and for longer ratchet lengths.

3.4 Time-Averaged Flow Fields

The time averaged flow fields (see Figs. 8 and 9) show that for the longer ratchets $\ell/k \geq 8$ less flow separation occurs for the windward oriented ratchets, since the mean flow field can conform to the gentle leeward slope of the ratchets. In contrast, a significant separated flow region can be observed in the time-averaged flow fields for the leeward oriented ratchets. The higher extent of the separated flow region for the leeward oriented cases can also be observed from the time-averaged mean streamwise velocity profiles within the ratchet cavities (see Fig.

7d), where reverse flow can be observed up to higher values of z/δ for the leeward oriented ratchets compared to their windward oriented counterparts.

The lower level of separation for the windward oriented cases promotes interaction between the mean flow and the steep windward section of the roughness which can thus impart a higher wall-normal momentum to the local mean flow. These variations in the time-averaged flow field can be quantified using the dispersive stresses, which are based on the spatial variations in the streamwise and wall-normal component in the averaged velocity field

$$\tilde{u}(x,z) = \overline{u}(x,z) - \langle \overline{u} \rangle (z), \tag{6}$$

$$\tilde{w}(x,z) = \overline{w}(x,z) - \langle \overline{w} \rangle (z), \tag{7}$$

where $\langle \cdot \rangle$ indicates the spatial average over x and $\overline{\cdot}$ the average over all aspects for which the flow is statistically independent, namely the average over time, the spanwise direction, and the spatial phases, i.e., the ratchet repetitions. The wall-normal dispersive stresses $\langle \tilde{w}\tilde{w} \rangle$ show consistently higher levels above the roughness crests for the windward oriented cases with $\ell/k \geq 8$ compared to their leeward oriented counterparts (see Fig. 7c); in addition, high levels of $\langle \tilde{w}\tilde{w} \rangle$ extend further into the flow for windward oriented ratchets. Similarly, higher levels of streamwise dispersive stresses $\langle \tilde{u}\tilde{u} \rangle$ (see Fig. 7b) are observed for the

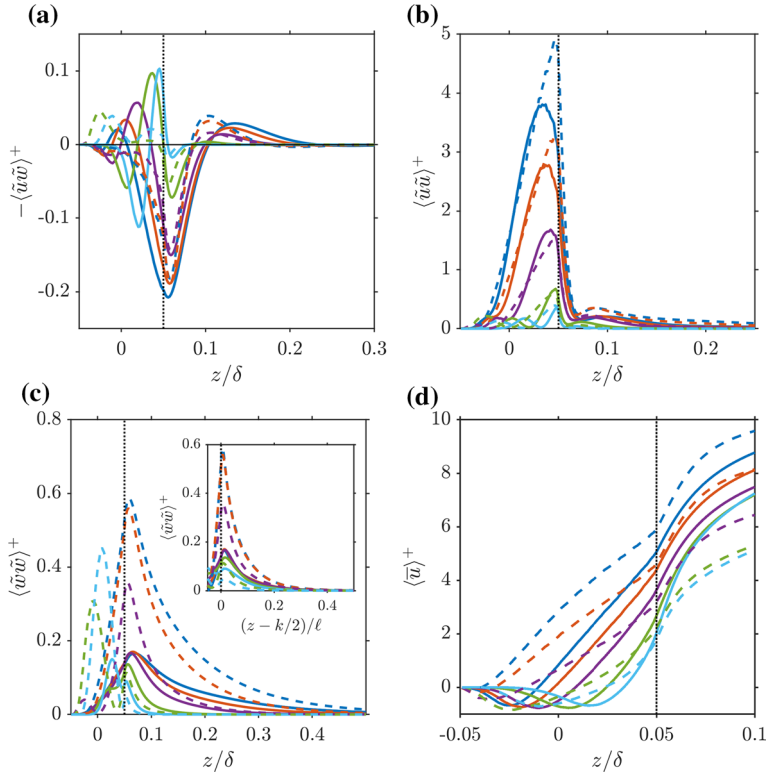

Fig. 7 Profiles of (**a**) dispersive shear stress; (**b**) streamwise dispersive stress; (**c**) wall-normal dispersive stress. (**d**) Mean velocity profiles very close to the rough wall and within the ratchet cavities. Line styles and symbols as shown in Table 1. The thin dotted vertical line indicates the height of the roughness crests

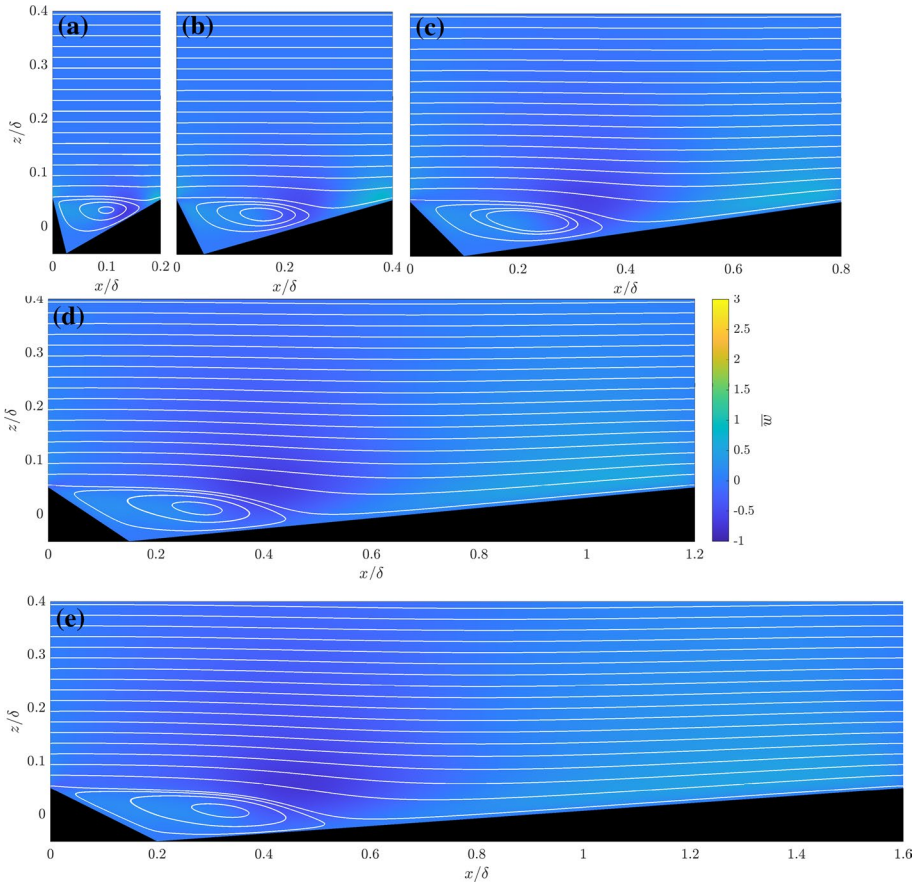

Fig. 8 Streamlines in time- and phase averaged mean flow fields for ratchets in leeward orientation. The background is shaded with the time- and phase-averaged wall-normal velocity component $\overline{w}$. (**a**) $\ell/k = 2$, (**b**) $\ell/k = 4$, (**c**) $\ell/k = 8$, (**d**) $\ell/k = 12$, and (**e**) $\ell/k = 16$

windward oriented cases compared to the leeward oriented cases, however, high levels for $\langle\tilde{u}\tilde{u}\rangle$ occur only within cavities of the ratchet surfaces, and $\langle\tilde{u}\tilde{u}\rangle$ drops to low levels above for all cases.

More complex behaviour emerges for the shorter ratchets with $\ell/k = 2$ and 4. Here the ratchet cavity is mostly occupied by a large vortex in both leeward and windward orientations. However, there is still an observable difference in the wall-normal extent of the separated flow regions, which reach to slightly higher z/δ values for the leeward oriented ratchets.

It should be noted that higher levels for $\langle\tilde{w}\tilde{w}\rangle$ do not necessarily translate to higher levels for the dispersive shear stress $-\langle\tilde{u}\tilde{w}\rangle$. As can be observed from the dispersive stress profiles (see Fig. 7a), the leeward oriented ratchets induce dispersive shear stress levels of similar magnitude or higher as the corresponding windward oriented ratchets. However, above the rough surface the trend of decreasing streamwise and wall-normal dispersive stress levels with decreasing ratchet length also holds for the dispersive shear stress.

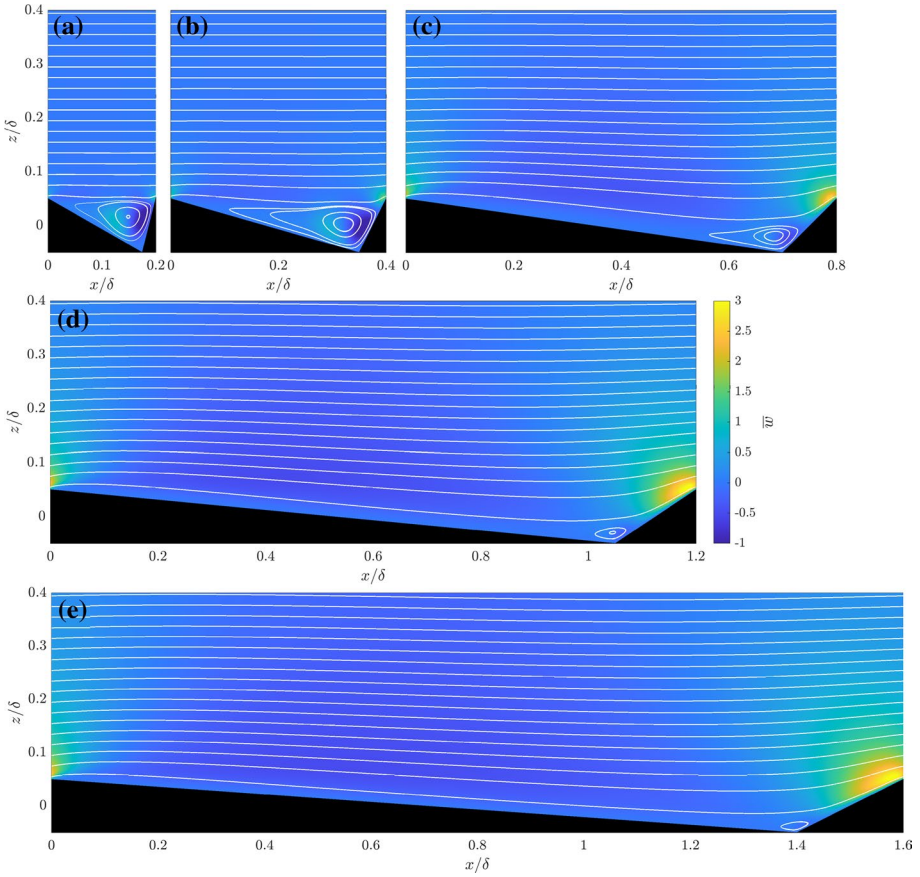

Fig. 9 Streamlines in time- and phase averaged mean flow fields for ratchets in windward orientation. The background is shaded with the time- and phase-averaged wall-normal velocity component $\overline{w}$. (**a**) $\ell/k = 2$, (**b**) $\ell/k = 4$, (**c**) $\ell/k = 8$, (**d**) $\ell/k = 12$, and (**e**) $\ell/k = 16$

Chan et al. (2018) found for 3D sinusoidal rough surfaces that the wall-normal dispersive stress levels above the roughness scaled with the transverse wavelength for fixed roughness height. Similarly, Sharma and García-Mayoral (2020) observed for dense canopies of filaments that the wall-normal extent of the influence of the canopy-induced flow was determined by the spacing between the filaments. For the present surfaces, the transverse wavelength is infinite, but we can consider the influence of the streamwise wavelength, i.e., the ratchet length ℓ. When plotting the wall-normal dispersive stress profiles against the wall-normal distance from the roughness crest $z - k/2$ scaled by ℓ (see inset in Fig. 7c), we find an excellent collapse of the profiles for the longer ratchets in leeward orientation ($\ell = 8k$, $12k$, and $16k$) above the rough surface. A very good collapse in this scaling is also observed between the two longest ratchets in windward orientation, but their collapsed profile remains distinct from the collapsed profile for the long leeward-oriented ratchets. The profiles for the shorter ratchets show deviations from the collapsed profiles for the longer ratchets, these deviations are higher for

ratchets in windward orientation and become stronger for shorter ratchet length. In all cases, wall-normal shear stress levels are negligible for $(z - k/2) \gtrapprox 0.3\ell$.

Overall, streamline patterns for the time-averaged flow fields show some similarities to observations for transverse bar roughness by Leonardi et al. (2003). For short cavity width-to-height ratio, a single vortex occupies almost the entire cavity, whereas the flow is attached over larger sections of the cavity walls for the longer cavities. However, due to the triangular cross-section of the current cavities compared to the rectangular cross-section for cavities between transverse bar roughness, there are also qualitative differences, especially for the longer cavities - for example, for the current cases, there is only single a separated region and for longer ratchets the flow is attached upstream and downstream of this separated region. In contrast, for transverse bar roughness with long spacing, there are two separated flow regions with an attached region at the cavity bottom in between.

Based on the observations made for the wall-normal component of the averaged flow field, we would expect that the turbulent velocity fluctuations also show higher spatial variations for the windward oriented cases. However, as can be observed from the turbulent kinetic energy fields shown in Figs. 10 and 11, the leeward oriented ratchets tend to induce higher spatial variations in the turbulent kinetic energy. This is because in the detached flow regions in the mean flow, turbulent kinetic energy levels are overall very low, and high levels of turbulent kinetic energy emerge over the gradual upslope sections of the leeward cavities. In contrast, for windward oriented ratchets, the turbulent kinetic energy is distributed more uniformly for a given wall-normal location. This may be why the roughness effect of the leeward oriented surfaces is still appreciable, even in view of a comparably weak interaction of the time-averaged flow with the upstream slope of the ratchets.

4 Conclusions

The orientation of ratchet-type rough surfaces has a significant influence on their effect on turbulent channel flow. For the roughness function, this effect is more prominent for the shorter ratchet lengths $\ell \leq 8k$. The mean velocity profile, Reynolds stresses, and the time-averaged flow fields show clear orientation dependency for all ratchet lengths considered.

Two empirical relationships that relate the roughness effect to surface-slope based topographical parameters were tested. However, neither the relationship by Sigal and Danberg (Sigal and Danberg 1990) for predicting the equivalent sand-grain roughness nor the empirical relationship by De Marchis et al. (De Marchis et al. 2020) for predicting the roughness function give a satisfactory prediction for the roughness effect of ratchet-type surfaces. Therefore, to account for the effect of orientation-dependency new empirical relationships need to be developed or existing relationships modified.

Mean flow and turbulence statistics show that ratchet orientation affects not only the roughness function, but every aspect of the flow, including levels of outer layer similarity, Reynolds and dispersive stress levels, and the spatial distribution of turbulent kinetic energy. The streamline patterns of the averaged velocity fields for the longer ratchet cases strongly depend on the ratchet orientation. Strong separation of the flow is observed over the steep leeward flank of the leeward oriented ratchets. In contrast, the flow can follow the more gradual downward leeward slope of the windward-oriented ratchets much better, but then encounters steep windward slope which induces a strong local upward motion of the mean flow resulting in a stronger effect of the ratchet pattern on the outer flow. For the long ratchets in leeward orientation, the highest turbulent kinetic energy levels are associated

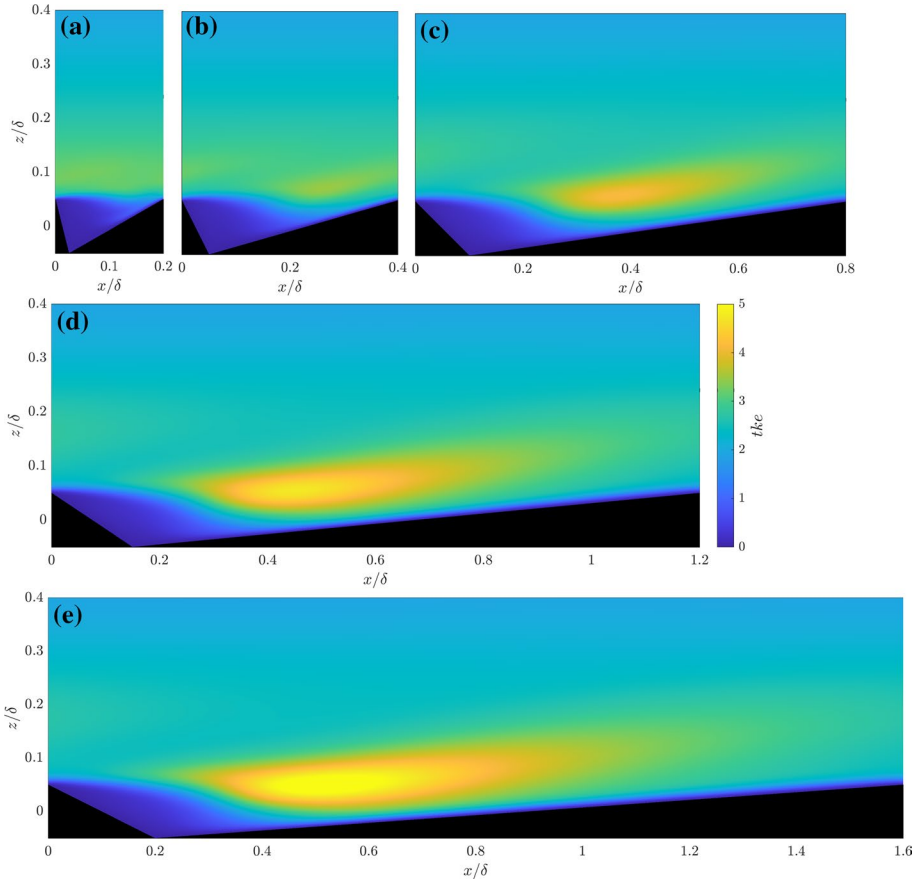

Fig. 10 Time and phase averaged turbulent kinetic energy for ratchets in leeward orientation. (**a**) $\ell/k = 2$, (**b**) $\ell/k = 4$, (**c**) $\ell/k = 8$, (**d**) $\ell/k = 12$, and (**e**) $\ell/k = 16$

with the reattachment of the separated shear layer that forms over the separated flow that is induced by the high leeward slope of the surface. No elevated turbulent kinetic energy values can be observed above the roughness crest. In contrast, for the long ratchets in windward orientation, the highest turbulent kinetic energy levels occur in a narrow attached flow region where the flow is deflected upward over the high windward slope section of the surface. This strong upward deflection also contributes to the higher wall-normal dispersive stress levels above the roughness for long ratchets in windward orientation. For shorter ratchets we observe a similar orientation-dependent effect on the mean velocity profile, but the structure of averaged velocity field and the spatial distribution of the turbulent kinetic energy is not as strongly orientation-dependent.

These results demonstrate that two-dimensional transverse roughness, which has been predominantly studied for transverse square bar roughness, is not yet fully understood and that further two-dimensional transverse roughness forms should be considered in future studies. In the context of ratchet roughness, it would for example be of interest to investigate the effect of the ratchet height k/δ on the virtual origin, e.g., by conducting simulations for the same k^+ but at higher Re_τ thus lowering the k/δ ratio.

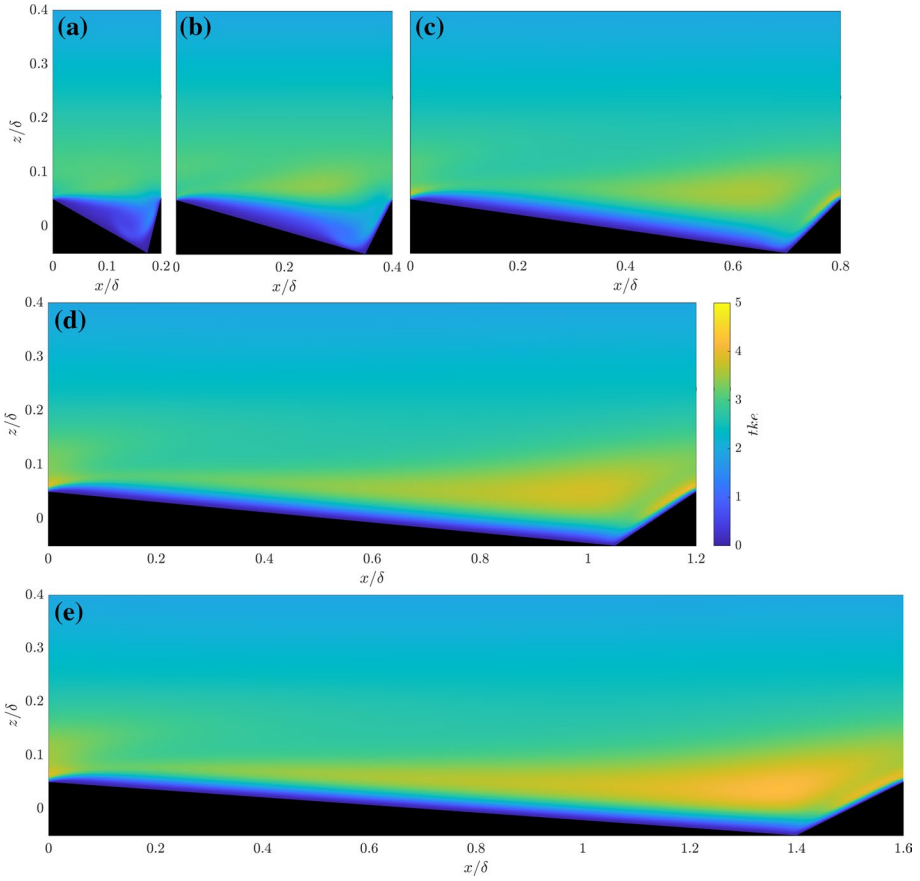

Fig. 11 Time and phase averaged turbulent kinetic energy for ratchets in windward orientation. (**a**) $\ell/k = 2$, (**b**) $\ell/k = 4$, (**c**) $\ell/k = 8$, (**d**) $\ell/k = 12$, and (**e**) $\ell/k = 16$

Even shorter ratchets could be considered to explore the scaling of the equivalent sand grain roughness with frontal solidity in the very high frontal solidity ('very dense' (MacDonald et al. 2018)) regime. Finally, the effect of different ratchet forms should be considered, e.g., by varying the b/ℓ ratio, to determine how strong a departure from an equilateral triangle cross-section ($b/\ell = 1/2$) is required to induce significant orientation dependency.

Acknowledgements We gratefully acknowledge support by the Engineering and Physical Sciences Research Council under grant numbers EP/V002066/1 and EP/P009875/1. This work used the Cirrus UK National Tier-2 HPC Service at EPCC (http://www.cirrus.ac.uk) funded by the University of Edinburgh and EPSRC (EP/P020267/1). A.B. gratefully acknowledges support via a Leverhulme Trust Research Fellowship. Velocity data are openly available from the University of Glasgow Enlighten repository under https://doi.org/10.5525/gla.researchdata.1318.

Declarations

Conflicts of interest The authors declare that they have no conflict of interest.

References

Busse, A., Jelly, T.O.: Influence of surface anisotropy on turbulent flow over irregular roughness. Flow Turbul. Combust. **104**, 331–354 (2020). https://doi.org/10.1007/s10494-019-00074-4

Busse, A., Lützner, M., Sandham, N.D.: Direct numerical simulation of turbulent flow over a rough surface based on a surface scan. Comput. Fluids **116**, 1290147 (2015). https://doi.org/10.1016/j.compfluid.2015.04.008

Busse, A., Thakkar, M., Sandham, N.D.: Reynolds-number dependence of the near-wall flow over irregular rough surfaces. J. Fluid Mech. **810**, 196–224 (2017). https://doi.org/10.1017/jfm.2016.680

Chan, L., MacDonald, M., Chung, D., Hutchins, N., Ooi, A.: A systematic investigation of roughness height and wavelength in turbulent pipe flow in the transitionally rough regime. J. Fluid Mech. **771**, 743–777 (2015). https://doi.org/10.1017/jfm.2015.172

Chan, L., MacDonald, M., Chung, D., Hutchins, N., Ooi, A.: Secondary motion in turbulent pipe flow with three-dimensional roughness. J. Fluid Mech. **854**, 5–33 (2018). https://doi.org/10.1017/jfm.2018.570

Chung, D., Hutchins, N., Schultz, M.P., Flack, K.A.: Predicting the drag of rough surfaces. Annu. Rev. Fluid Mech. **53**(1), 439–471 (2021). https://doi.org/10.1146/annurev-fluid-062520-115127

De Marchis, M.: Large eddy simulations of roughened channel flows: Estimation of the energy losses using the slope of the roughness. Comput. Fluids **140**, 148–157 (2016). https://doi.org/10.1016/j.compfluid.2016.09.021

De Marchis, M., Saccone, D., Milici, B., Napoli, E.: Large eddy simulations of rough turbulent channel flows bounded by irregular roughness: Advances toward a universal roughness correlation. Flow Turbul. Combust. **105**(2), 627–648 (2020). https://doi.org/10.1007/s10494-020-00167-5

Flack, K.A., Schultz, M.P.: Roughness effects on wall-bounded turbulent flows. Phys. Fluids **26**, 101305 (2014). https://doi.org/10.1063/1.4896280

Forooghi, P., Stroh, A., Magagnato, F., Jakirlić, S., Frohnapfel, B.: Toward a universal roughness correlation. J. Fluids Eng. **139**(12), 121201 (2017). https://doi.org/10.1115/1.4037280

Forooghi, P., Stroh, A., Schlatter, P., Frohnapfel, B.: Direct numerical simulation of flow over dissimilar, randomly distributed roughness elements: A systematic study on the effect of surface morphology on turbulence. Phys. Rev. Fluids **3**(4), 044605 (2018). https://doi.org/10.1103/PhysRevFluids.3.044605

Gao, X., Narteau, C., Rozier, O.: Development and steady states of transverse dunes: A numerical analysis of dune pattern coarsening and giant dunes. J. Geophys. Res. Earth Surf. **120**(10), 2200–2219 (2015). https://doi.org/10.1002/2015JF003549

Hama, F.R.: Boundary-layer characteristics for smooth and rough surfaces. Trans. Soc. Naval Archit. Mar. Eng. **62**, 333–351 (1954)

Jelly, T.O., Busse, A.: Reynolds number dependence of Reynolds and dispersive stresses in turbulent channel flow past irregular near-Gaussian roughness. Int. J. Heat Fluid Flow **80**, 108485 (2019). https://doi.org/10.1016/j.ijheatfluidflow.2019.108485

Jiang, H., Zhu, X., Mathai, V., Verzicco, R., Lohse, D., Sun, C.: Controlling heat transport and flow structures in thermal turbulence using ratchet surfaces. Phys. Rev. Lett. **120**(4), 044501 (2018). https://doi.org/10.1103/PhysRevLett.120.044501

Jiménez, J.: Turbulent flow over rough walls. Ann. Rev. Fluid Mech. **36**, 173–96 (2004). https://doi.org/10.1146/annurev.fluid.36.050802.122103

Krogstad, P.-Å., Efros, V.: About turbulence statistics in the outer part of a boundary layer developing over two-dimensional surface roughness. Phys. Fluids **24**(7), 075112 (2012). https://doi.org/10.1063/1.4737658

Kuwata, Y., Nagura, R.: Direct numerical simulation on the effects of surface slope and skewness on rough-wall turbulence. Phys. Fluids **32**(10), 105113 (2020). https://doi.org/10.1063/5.0024038

Leonardi, S., Orlandi, P., Smalley, R.J., Djenidi, L., Antonia, R.A.: Direct numerical simulations of turbulent channel flow with transverse square bars on one wall. J. Fluid Mech. **491**, 229–238 (2003). https://doi.org/10.1017/S0022112003005500

Longuet-Higgins, M.S.: On the skewness of sea-surface slopes. J. Phys. Oceanogr. **12**(11), 1283–1291 (1982). https://doi.org/10.1175/1520-0485(1982)012<1283:OTSOSS>2.0.CO;2

Macdonald, R.W., Griffiths, R.F., Hall, D.J.: An improved method for the estimation of surface roughness of obstacle arrays. Atmos. Environ. **32**(11), 1857–1864 (1998). https://doi.org/10.1016/S1352-2310(97)00403-2

MacDonald, M., Chan, L., Chung, D., Hutchins, N., Ooi, A.: Turbulent flow over transitionally rough surfaces with varying roughness densities. J. Fluid Mech. **804**, 130–161 (2016). https://doi.org/10.1017/jfm.2016.459

MacDonald, M., Ooi, A., García-Mayoral, R., Hutchins, N., Chung, D.: Direct numerical simulation of high aspect ratio spanwise-aligned bars. J. Fluid Mech. **843**, 126–155 (2018). https://doi.org/10.1017/jfm.2018.150

Napoli, E., Armenio, V., De Marchis, M.: The effect of the slope of irregularly distributed roughness elements on turbulent wall-bounded flows. J. Fluid Mech. **613**, 385–394 (2008). https://doi.org/10.1017/S0022112008003571

Pope, S.B.: Turbulent Flows. Cambridge University Press, Cambridge (2000)

Sarakinos, S., Busse, A.: Investigation of rough-wall turbulence over barnacle roughness with increasing solidity using direct numerical simulations. Phys. Rev. Fluids **7**(6), 064602 (2022). https://doi.org/10.1103/PhysRevFluids.7.064602

Schlichting, H.: Experimentelle Untersuchungen zum Rauhigkeitsproblem. Ingenieur-Archiv **7**, 1–34 (1936)

Schultz, M.P., Flack, K.A.: Turbulent boundary layers on a systematically varied rough wall. Phys. Fluids **21**, 015104 (2009). https://doi.org/10.1063/1.3059630

Seyed-Aghazadeh, B., Carlson, D.W., Modarres-Sadeghi, Y.: Vortex-induced vibration and galloping of prisms with triangular cross-sections. J. Fluid Mech. **817**, 590–618 (2017). https://doi.org/10.1017/jfm.2017.119

Sharma, A., García-Mayoral, R.: Turbulent flows over dense filament canopies. J. Fluid Mech. **888**, A2 (2020). https://doi.org/10.1017/jfm.2020.27

Sigal, A., Danberg, J.E.: New correlation of roughness density effect on the turbulent boundary layer. AIAA J. **28**(3), 554–556 (1990). https://doi.org/10.2514/3.10427

Thakkar, M., Busse, A., Sandham, N.D.: Surface correlation of hydrodynamic drag for transitionally rough engineering surfaces. J. Turbul. **138**, 138–169 (2017). https://doi.org/10.1080/14685248.2016.1258119

Thakkar, M., Busse, A., Sandham, N.D.: Direct numerical simulation of turbulent channel flow over a surrogate for Nikuradse-type roughness. J. Fluid Mech. (2018). https://doi.org/10.1017/jfm.2017.873

van Rij, J.A., Belnap, B.J., Ligrani, P.M.: Analysis and experiments on three-dimensional, irregular surface roughness. J. Fluids Eng. **124**, 671 (2002). https://doi.org/10.1115/1.1486222

Yang, J., Balaras, E.: An embedded-boundary formulation for large-eddy simulation of turbulent flows interacting with moving boundaries. J. Comput. Phys. **215**, 12 (2006). https://doi.org/10.1016/j.jcp.2005.10.035